Inorganic Chemistry

pubs.acs.org/IC Article

Distinguishing the Intrinsic Antiferromagnetism in Polycrystalline $LiCoPO_4$ and $LiMnPO_4$ Olivines

Stephanie Gnewuch and Efrain E. Rodriguez*

Cite This: https://dx.doi.org/10.1021/acs.inorgchem.9b03545 Read Online

ACCESS | Metrics & More | Article Recommendations | Supporting Information

ABSTRACT: We report a detailed investigation of the long-range magnetic ordering in polycrystalline samples of $LiCoPO_4$ and $LiMnPO_4$, which belong to a series of well-known olivine cathode materials $LiMPO_4$ (M = Mn, Fe, Co, Ni). Samples were prepared by hydrothermal and solid state methods. The magnetic susceptibility is found to be strongly field-dependent, impacting the antiferromagnetic transition temperature and the bifurcation of the FC and ZFC curves. We discuss the role synthesis conditions have on impurity formation and particle size. We report neutron powder diffraction data for the samples prepared by solid state methods. Based upon representational analysis of the observed reflections, we affirm the magnetic structure *Pnma′* for $LiCoPO_4$ and *Pn′m′a′* for $LiMnPO_4$. The refined magnetic moments from these models are 3.28(4) μ_B for $LiCoPO_4$ and 4.28(3) μ_B for $LiMnPO_4$. We also study the onset of magnetic ordering in each sample and affirm that the ordering temperature is 22 K for $LiCoPO_4$ and 34 K for $LiMnPO_4$. The critical parameters describing those transitions are β_c = 0.21(4) ($LiCoPO_4$) and β_c = 0.31(3) ($LiMnPO_4$). These values are characteristic of a 3D Ising system for $LiMnPO_4$ and intermediate behavior between a 2D and 3D Ising system for $LiCoPO_4$. We compare these observations with other reports proposing lower magnetic symmetry.

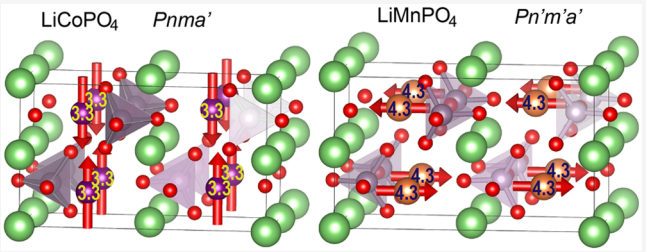

INTRODUCTION

The $LiMPO_4$ (M = Mn, Fe, Co, Ni) olivine series and their solid solutions are electrochemically active materials which display long-range antiferromagnetic order below their transition temperatures. Most investigations on these materials have focused on their electrochemistry, since their reversible lithium ion extraction can be controlled in an electrochemical cell.[1−7] Their magnetic point group symmetry permits a linear magneto-electric effect in these compositions, and several authors have proposed mechanisms for how their response under applied fields is impacted by their ordering.[8−11] The magnetic structure of $LiCoPO_4$ has been scrutinized in particular, since it was found to have the highest magneto-electric coefficient of the series.[12,13]

Both their electrochemical activity and magnetic ordering arise from their structural features. The olivine structure type $B_2(AO_4)$ belongs to the large AB_2O_4 group of complex oxides, where AO_4 is a tetrahedral oxyanion.[14] Chrysoberyl, spinel, and phenacite are also members of the AB_2O_4 group, classified according to their close packing, occupation of the tetrahedral and octahedral holes, and the oxidation states of the A and B ions.[14] In olivines, the complex anion is most commonly silicate or phosphate, although a number of other tetrahedral anions have been observed. The tetrahedral anions do not share any edges or vertices with one another.[15] Rather, the anions form octahedral polyhedra around the A and B cation sites (Figure 1). The oxyanion plays a dual role in the $LiMPO_4$ (M = Mn, Fe, Co, Ni) series. The oxyanion framework forms channels of distorted octahedra around the lithium sites, which facilitate the lithium intercalation during the oxidation and reduction of the transition metal.[16] The oxyanions also facilitate the superexchange interactions between the transition metal cations, which defines their magnetic ordering.[17]

The magnetically ordered domains in the cobalt and nickel members have been studied extensively by Schmid et al.[19−21] They notably discovered that the behavior of the domains in $LiCoPO_4$ under magnetic and electric fields was characteristic of ferrotoroidal order. Ferrotoroidics are a class of primary ferroics where the magnetic moments antialign in pairs to give rise to long-range ordering of toroidal moments normal to the pairs. Controlling such domains would have broader applications in magnetic memory storage.[12,22,23]

As with all magnetic materials, the symmetry of the magnetic point group dictates the symmetry of the physical property tensors. The magnetic structure models for $LiCoPO_4$ and $LiMnPO_4$ were first proposed by Santoro, Newnham, and their respective colleagues in the 1960s.[24−26] However, later neutron diffraction and second harmonic generation experiments on

Received: December 5, 2019

https://dx.doi.org/10.1021/acs.inorgchem.9b03545
Inorg. Chem. XXXX, XXX, XXX−XXX

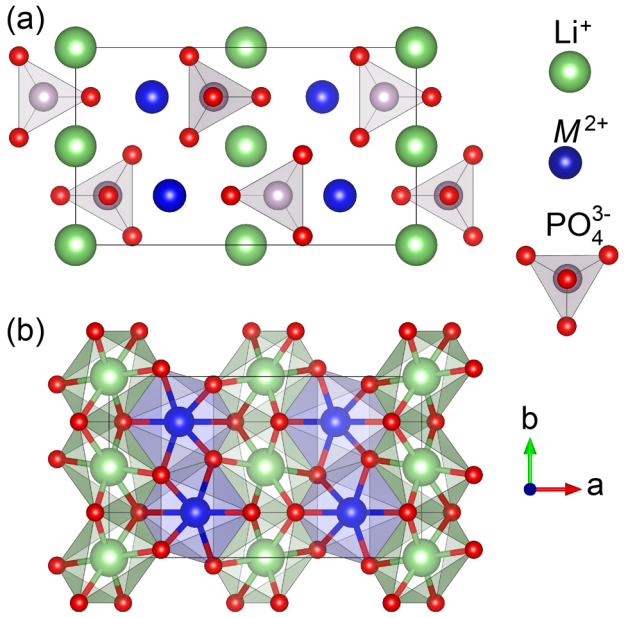

Figure 1. Structural model of Li*M*PO_4, with the tetrahedral phosphate arrangement depicted in (a) and octahedra sites occupied by the cations in b. Both images are viewed along the *c* axis. The phosphate ions are omitted in (b) for clarity. The images were created using the modeling software *VESTA 3*.[18]

single crystals of $LiCoPO_4$ have uncovered evidence for lower magnetic point symmetry.[19,21,27−29] This is detailed in the Discussion section.

Our purpose for undertaking this work was to fully characterize the spontaneous magnetic ordering of polycrystalline samples of $LiCoPO_4$ and $LiMnPO_4$. In particular, we address the inconsistencies in reported magnetic susceptibility measurements by examining samples prepared via two different synthetic methods and measured under various experimental conditions. We conclude that the behavior observed in polycrystalline samples is dependent upon applied field. We also observe differences in the synthetic method that we ascribe to particle size and low levels of impurities. We also report the long-range antiferromagnetic structure of these two compounds from neutron powder diffraction data and discuss these results in the context of recent work by other research groups.

EXPERIMENTAL SECTION

Solid State Synthesis. The so-called "solid state samples" were prepared using conventional ceramic sintering techniques. The reagents and heating profiles described herein were inspired by those which Baker, Kellerman, and their respective coauthors used.[30,31] All reagents were reagent-grade and used without further purification.

$LiMnPO_4$ was prepared on a 4 g scale from stoichiometric portions of manganese(II) oxide (Alfa Aesar), ammonium dihydrogen phosphate (Fisher Sci.), and lithium carbonate (Honeywell). The reagents were ground in ethanol with an agate mortar and pestle to form a homogeneous paste. Excess ethanol was allowed to evaporate under ambient conditions before the damp powder was transferred to an alumina crucible. Heating was performed in a tube furnace under argon flow gas placed inside a fume hood. The heating profile was set to ramp to 800 °C at 300 °C/h, to dwell for 12−14 h, and then to naturally cool to room temperature. The light tan-colored product was reground and pelletized before repeating the heating profile.

$LiCoPO_4$ was prepared at a 5 g scale from cobalt(II,III) oxide (Alfa Aesar), ammonium dihydrogen phosphate (Fisher Sci.), and lithium carbonate (Honeywell). The reagents were similarly ground before heating in an alumina crucible under ambient conditions in a box furnace placed inside a fume hood. The initial heating was performed at 375 °C for 2 h before the sample was naturally cooled to room temperature for regrinding. The second heating was performed at 800 °C for 12 hours. The product was bright purple.

Hydrothermal Synthesis. A second set of samples was prepared by hydrothermally treating precipitated metal phosphate precursors in 45 mL Teflon-lined Parr acid digestion vessels. This set will be referred to as the "hydrothermal" samples. Based upon the investigation by Lu et al.,[32] citric acid, ammonium hydroxide, and argon purge gas were used to protect the transition metal ions from oxidation. The heating conditions were chosen based upon optimization studies performed by Manzi and co-workers.[33,34] The reagents were reagent-grade and used as received. The water was deionized in-house through reverse osmosis and then vigorously bubbled with argon gas for 30 min immediately prior to use. Quantities of reagents were calculated based upon 0.01 mol of phosphate in a ratio of 1 transition metal cation:1 phosphate:1.5 lithium ion:0.04 citrate.

Ammonium phosphate monobasic (Fisher Scientific), citric acid (Sigma-Aldrich), and cobalt(II) sulfate heptahydrate (Alfa Aesar; or manganese(II) sulfate monohydrate (Alfa Aesar)) were dissolved in a few milliliters of water under flowing argon. Lithium hydroxide (Alfa Aesar) was dissolved under ambient conditions in a separate portion of water before being added to the first solution with vigorous swirling. As the precursors quickly precipitate, a solution of 10-fold dilute ammonium hydroxide solution (BDH) is added dropwise until the pH is between 6.0 and 7.5. Typically, 2 to 3 mL are required. Additional water is then added to obtain a final total volume of 23.0 mL. The thickened mixture is rapidly transferred to the Teflon sleeve and bubbled with argon for at least 60 s to purge the headspace before sealing. The vessels were placed in a preheated oven at 220 °C set to dwell for 10 h and then naturally cooled. The product is filtered, washed repeatedly with water, and allowed to dry under ambient conditions. This yields ∼0.5 g of bright purple ($LiCoPO_4$) or light tan ($LiMnPO_4$) product.

Powder Diffraction. Laboratory X-ray powder diffraction data were collected on a Bruker D8 Advance diffractometer equipped with a LynxEye detector. Experiments were performed at room temperature with Cu Kα radiation ($\lambda_{\alpha 1}$ = 1.54059 Å, $\lambda_{\alpha 2}$ = 1.54443 Å).

The solid state samples were selected for neutron diffraction experiments, since over three grams of sample were produced per batch. The samples were analyzed on the constant wavelength diffractometer BT-1 at the NIST Center for Neutron Research (NCNR). Vanadium sample cans were filled with a 2.7 g portion of $LiMnPO_4$ and 4.5 g portion of $LiCoPO_4$ under a He atmosphere. The Ge(311) monochromator (λ = 2.079 Å) with 60′ collimation was chosen to maximize neutron flux and resolution at low angles. Measurements were taken at 10 K and above the transition temperature (30 K for $LiCoPO_4$, 50 K for $LiMnPO_4$). In addition, the (012) magnetic reflection (56.9° 2θ) was measured on $LiCoPO_4$ at 13 temperatures from 4.6 K to 32.2 K. Likewise the (010) magnetic reflection (19.6° 2θ) was measured at 17 temperatures from 10.0 K to 50.0 K for $LiMnPO_4$. All measurements were normalized to monitor counts.

Magnetic Susceptibility. Temperature-dependent magnetic susceptibility measurements were performed on a commercial SQUID magnetic property measurement system (MPMS, Quantum Design). For each sample, a measured portion around 100 mg was loaded into a gel capsule with cotton suspended inside a plastic straw. Field-cooled (FC) and zero field-cooled (ZFC) measurements were recorded in direct current mode from room temperature (300 K) to base temperature (2−5 K) at various fields. Field-dependent measurements were performed with applied fields between ±7 T at various temperatures above and below the Néel temperature. The fields and temperatures selected are indicated directly on the figure for each measurement.

https://dx.doi.org/10.1021/acs.inorgchem.9b03545
Inorg. Chem. XXXX, XXX, XXX−XXX

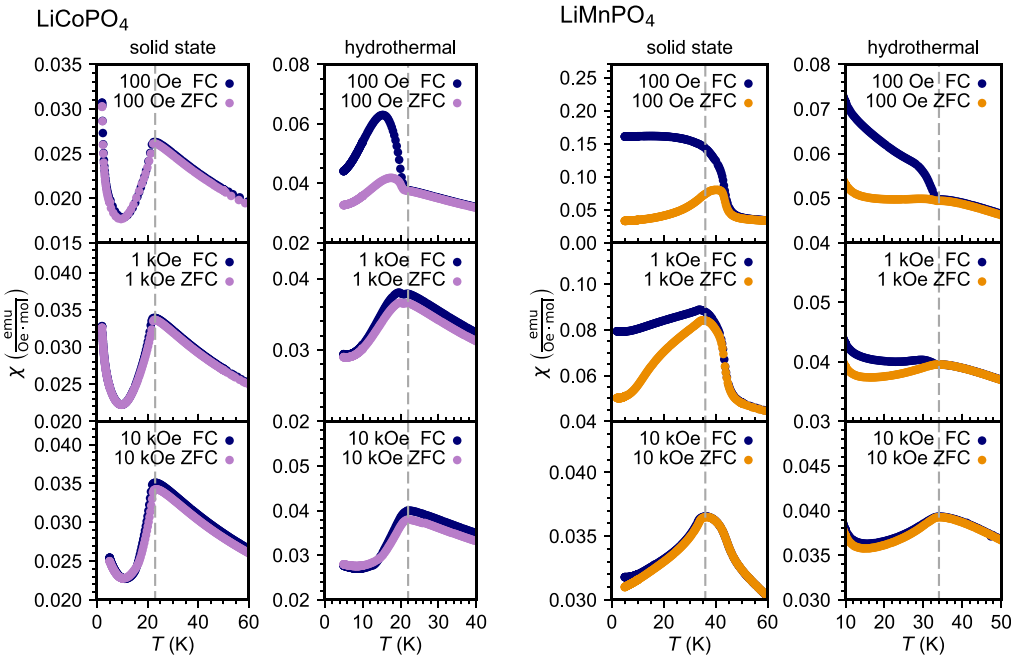

Figure 2. Temperature-dependent magnetic susceptibility of hydrothermal and solid state $LiCoPO_4$ and $LiMnPO_4$ at 100 Oe, 1 kOe, and 10 kOe. The dotted line indicates the Néel temperature presented in Table 1. It has been added to aid comparison of the measurements at different fields.

RESULTS

Preliminary Phase Identification. Simple preliminary structural refinements were performed on each of the X-ray diffraction patterns using the software TOPAS 5.[35] The $LiCoPO_4$ samples were fitted to the structural model reported by Kubel,[36] and the $LiMnPO_4$ to that of Urusova et al.[37] The only structural features refined were lattice parameters and crystallite size. All reflections could be indexed to the space group *Pnma* and are in good agreement with the calculated intensities. The refinements are included in Figure S1.

In general, the reflections in the X-ray diffraction patterns from hydrothermal samples are slightly broader and less intense than their solid state analogs, likely due to hydrothermal samples having a smaller particle size. The hydrothermal samples also tend to show strong preferred orientation along the *b* axis if the powders are packed into the sample holder before measurement.

For the samples measured in this work, no off-colored impurities were visually observed on the surface of the pellets for the solid state samples or in the filtered powders for hydrothermal samples. Nevertheless, low levels of impurities (<1%) are undetectable by laboratory X-ray powder diffraction.

Magnetic Susceptibility. To probe for parasitic signals from trace magnetic impurities, the magnetic susceptibility was measured for each of the samples under a variety of conditions.

Temperature-Dependent Magnetization at Constant Fields. The FC and ZFC temperature-dependent susceptibility around the paramagnetic to antiferromagnetic transition is presented in Figure 2 for the four samples at three different applied fields. The characteristic cusp for an antiferromagnetic transition is evident in the ZFC transitions for each of them. The Néel temperatures (T_N) presented in Table 1 are the temperatures at the cusp of the anomaly in each 10 kOe measurement. In all except the solid-state $LiCoPO_4$, the FC and ZFC curves diverge around the anomaly, but this signal is suppressed at higher magnetic fields. In addition, at higher fields the cusp shifts to a slightly higher temperature for hydrothermal $LiCoPO_4$ and a slightly lower temperature for solid state $LiMnPO_4$.

Table 1. Summary of the Curie–Weiss Fitting Parameters for $LiCoPO_4$ and $LiMnPO_4$ from Data Obtained with a 10 kOe Applied Field

	$LiCoPO_4$		$LiMnPO_4$	
	hyd[a]	ss[b]	hyd	ss
T_N (K)[c]	22(2)	24(2)	34(2)	36(2)
θ_{CW} (K)	−58(2)	−53(3)	−66(0)	−62(1)
C (emu·K/mol·Oe)	3.66(4)	3.24(7)	4.37(1)	3.84(4)
μ_{eff} (μ_B)	5.4(1)	5.1(1)	5.91(2)	5.54(6)
$\lvert\theta_{CW}\rvert/T_N$	2.6(3)	2.2(3)	1.9(1)	1.7(1)

[a]Sample prepared via a hydrothermal method. [b]Sample prepared via a solid state method. [c]An error of ±2 K was estimated based upon the number of data points measured around the transition temperature.

Note that in the hydrothermal $LiMnPO_4$ sample there is a strong positive signal which emerges below 10 K in the susceptibility. The strength of the signal obscures both the cusp of the susceptibility and FC/ZFC divergence due to data scaling and is therefore presented separately in Figure S2.

All samples exhibit a linear paramagnetic response at high temperatures, as shown in Figure 3. The high-temperature region (150–300 K) of the ZFC measurements was fitted with the Curie–Weiss equation:

$$\chi = \chi_0 + \frac{C}{(T - \theta_{CW})} \quad (1)$$

where θ_{CW} is the Curie–Weiss temperature and C is the Curie constant. The temperature-independent contributions to the susceptibility χ_0 (from the sample holder, etc.) were found to be negligibly small.

The slope of the inverse susceptibility (Figure 3) is noticeably lower at 100 Oe for hydrothermal $LiMnPO_4$ and slightly lower at 100 Oe and 1 kOe for solid state $LiMnPO_4$.

https://dx.doi.org/10.1021/acs.inorgchem.9b03545
Inorg. Chem. XXXX, XXX, XXX–XXX

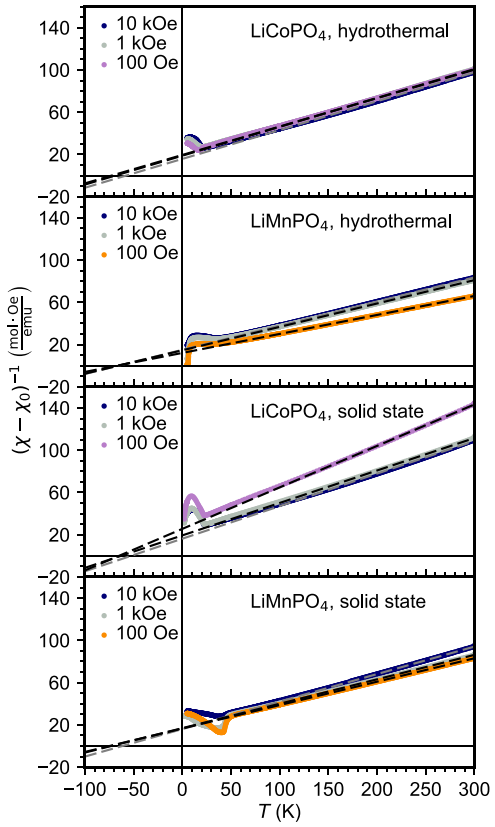

Figure 3. Inverse susceptibility of solid state and hydrothermal $LiCoPO_4$ and $LiMnPO_4$ fitted with the linear best fit lines fitted according to the Curie–Weiss law.

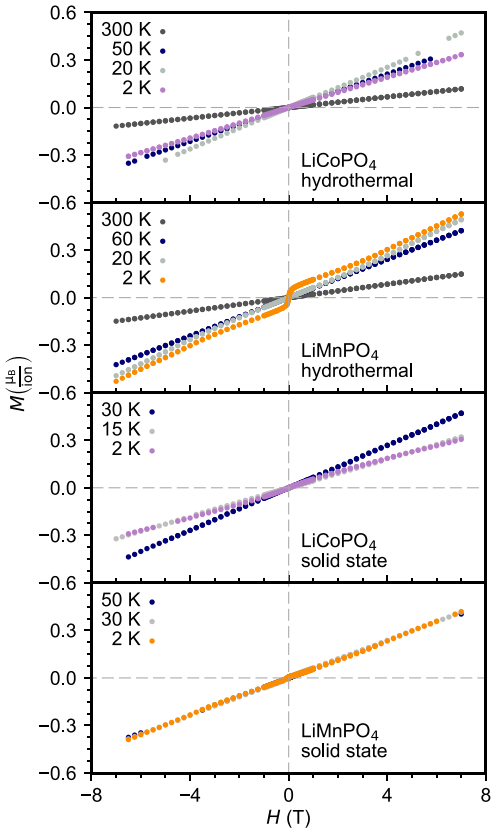

Figure 4. Field-dependent magnetic susceptibility of solid state and hydrothermal $LiCoPO_4$ and $LiMnPO_4$ at various temperatures above and below the Néel temperature.

This behavior is unsurprising for both $LiMnPO_4$ samples, since it is evident in Figure 2 and Figure S2 that the susceptibility is noticeably impacted by field.

At the same time, the slope of the inverse susceptibility for solid state $LiCoPO_4$ was noticeably higher at 100 Oe than at higher fields, without exhibiting FC/ZFC divergence (Figure 2). Because of this observed field dependence, only the fitting parameters for the data obtained with a 10 kOe applied field are included in Table 1. The calculated frustration parameter $|\theta_{CW}|/T_N$ and effective moment $\mu_{eff} = \sqrt{8C}$ are included in this Table 1 as well.

Field-Dependent Magnetization Isotherms. Field-dependent susceptibility was measured up to 7 T at a variety of temperatures above and below the transition. These data are presented in Figure 4.

Ferromagnetic remanence is clearly observed in the hydrothermal $LiMnPO_4$ sample at 2K. At the other temperatures measured, the field-dependent susceptibility appears linear. The low-field region of the 2 K data is depicted in more detail in Figure S3. There are not enough data to clearly resolve a coercive field in the measurement at 2 K. Such a field would be on the order of 100 Oe, which suggests the strong signal observed below 10 K in Figure S2 is from an unidentified ferri- or ferromagnetic impurity.

The measurements for the other samples appear linear. However, there is a subtle curvature in the solid state $LiCoPO_4$ measurement at 2 K, evidenced by its nonoverlap with the 15 K measurement. The same is true for the 2 K measurement of solid state $LiMnPO_4$ and hydrothermal $LiCoPO_4$. The data for the solid state $LiCoPO_4$ and $LiMnPO_4$ are presented in a larger plot in Figures S4 and S5. A very slight remanance is observable in the region below ±250 Oe. Again, not enough measurements were taken at such low fields to assign a coercive field.

Neutron Powder Diffraction. Neutron powder diffraction data of solid state $LiCoPO_4$ and $LiMnPO_4$ reveal a number of reflections that emerge at low temperature, which can be attributed to long-range magnetic ordering (Figure 5). Indexing and refinement were performed using the software GSAS-II.[38] Patterns for both compositions were indexed according to the space group *Pnma* to aid comparison between them. (Some early reports on $LiMnPO_4$ used the setting *Pmnb*.)

The starting model for the refinement of the 30 K measurement of $LiCoPO_4$ was fit using Kubel's reported structure.[36] For the 50 K measurement of $LiMnPO_4$, the structure chosen was reported by Urusova et al.[37] The refined crystallographic parameters are included in Table 2. The refined crystal structure models and bond lengths and angles are provided in Tables S2–S4.

For the measurements above the transition temperature, any reflections which cannot be indexed to the lithium transition metal orthophosphate are assumed to be an impurity phase. For the $LiMnPO_4$ sample, there was a noticeable reflection around 4.41 $Å^{-1}$, as well as a few low-intensity reflections around 2.82 $Å^{-1}$, 2.46 $Å^{-1}$, and 1.54 $Å^{-1}$ barely above the level of the background. With so few reflections, all attempts to identify the impurity phase were unsuccessful. Likewise for the $LiCoPO_4$ sample, weak reflections just above the level of the

https://dx.doi.org/10.1021/acs.inorgchem.9b03545
Inorg. Chem. XXXX, XXX, XXX−XXX

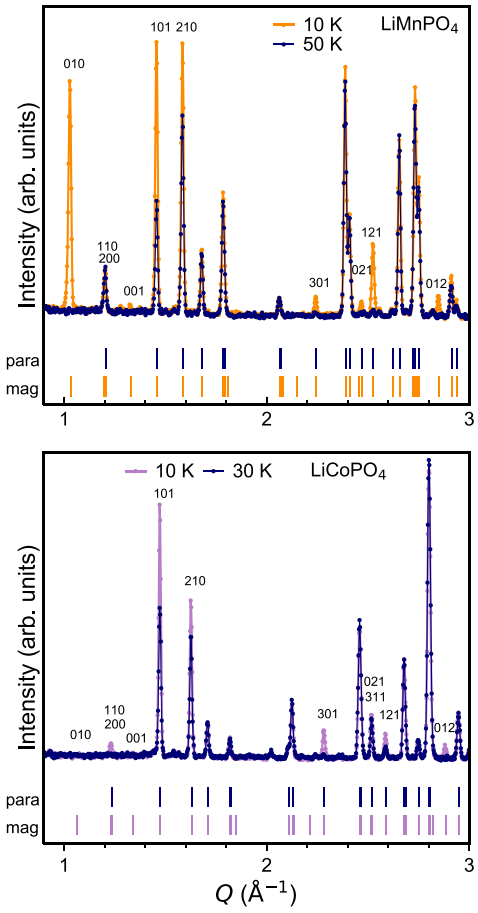

Figure 5. Indexed neutron powder diffraction patterns for $LiCoPO_4$ and $LiMnPO_4$ data taken at 10 K. The pattern taken above the Néel temperature (50 K for $LiMnPO_4$ and 30 K for $LiCoPO_4$) is overlaid to distinguish the intensity of the reflections in the 10 K pattern attributable to magnetic ordering. The tick marks for the paramagnetic (high-temperature) phase are labeled "para." Those for the magnetically ordered (10 K) phase are labeled "mag."

Table 2. Crystallographic Parameters of $LiCoPO_4$ and $LiMnPO_4$ Determined from Rietveld Refinement of Neutron Powder Diffraction Data

$LiMnPO_4$	50 K	10 K
S.G.	*Pnma*	*Pnma*
a (Å)	10.4270(3)	10.4264(3)
b (Å)	6.0915(2)	6.0909(2)
c (Å)	4.7309(1)	4.7310(1)
V (Å^3)	300.49(1)	300.45(1)
R_p	6.546%	6.547%
R_{wp}	9.486%	9.770%
GOF	1.762	1.888
$LiCoPO_4$	30 K	10 K
S.G.	*Pnma*	*Pnma*
a (Å)	10.1888(3)	10.1877(3)
b (Å)	5.9074(2)	5.9073(2)
c (Å)	4.6891(1)	4.6891(1)
V (Å^3)	282.23(1)	282.20(1)
R_p	6.688%	6.814%
R_{wp}	8.647%	8.805%
GOF	1.841	1.773

background were observed around 4.40 Å^{-1}, 3.10 Å^{-1}, 2.80 Å^{-1}, 2.02 Å^{-1}, and 1.54 Å^{-1}. These were also unidentified.

In addition to measuring the full patterns, we chose a prominent reflection at 10 K for each composition which only has contributions to the observed intensity from magnetic scattering. We chose the (012) reflection for $LiCoPO_4$ and the (010) reflection for $LiMnPO_4$. These reflections were monitored upon cooling across the transition temperature. The integrated intensity of the reflections is plotted versus temperature in Figure 6.

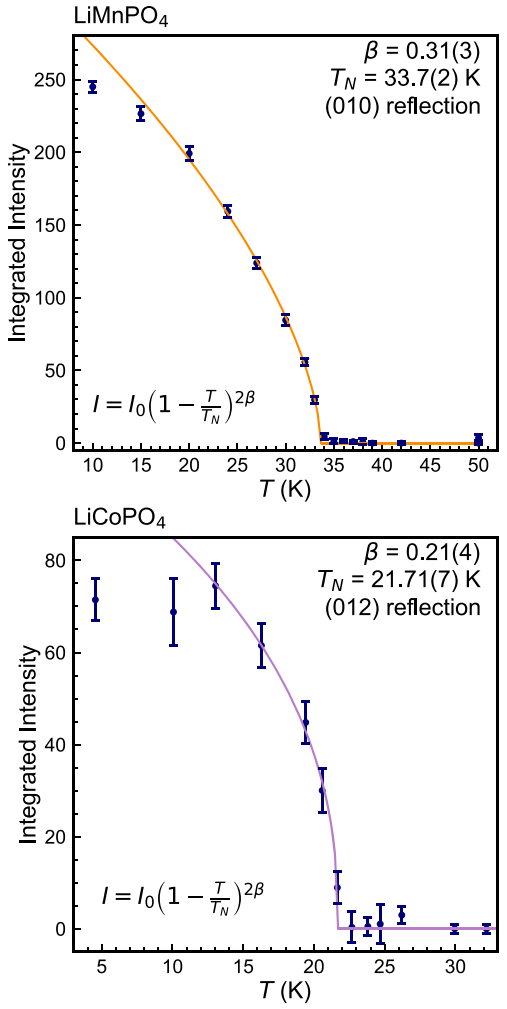

Figure 6. Temperature dependence of the integrated intensity of the (012) reflection of $LiCoPO_4$ and the (010) reflection of $LiMnPO_4$. Both data sets have been fit to a power law (eq 3).

When a system undergoes a transition from a paramagnetic state to an ordered magnetic state, that transition can be described according to an order parameter. For magnetic systems, this is the magnetization of the sublattice *M*. The magnetic reflection's integrated intensity *I* is dependent upon temperature according to the expression $M(T) \propto \sqrt{I(T)}$[39−41] and can be substituted into a power law:

$$\frac{M(T)}{M(0)} = A\left(1 - \frac{T}{T_N}\right)^{\beta} \quad (2)$$

https://dx.doi.org/10.1021/acs.inorgchem.9b03545
Inorg. Chem. XXXX, XXX, XXX−XXX

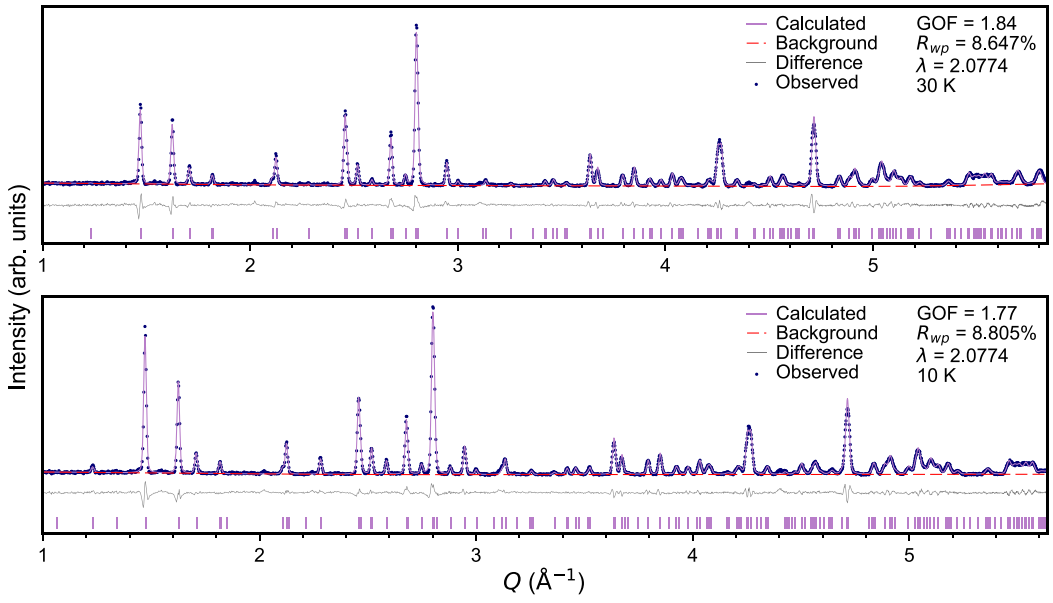

Figure 7. Refinements of the nuclear and magnetic structures with neutron powder diffraction data of $LiCoPO_4$ above and below the ordering temperature.

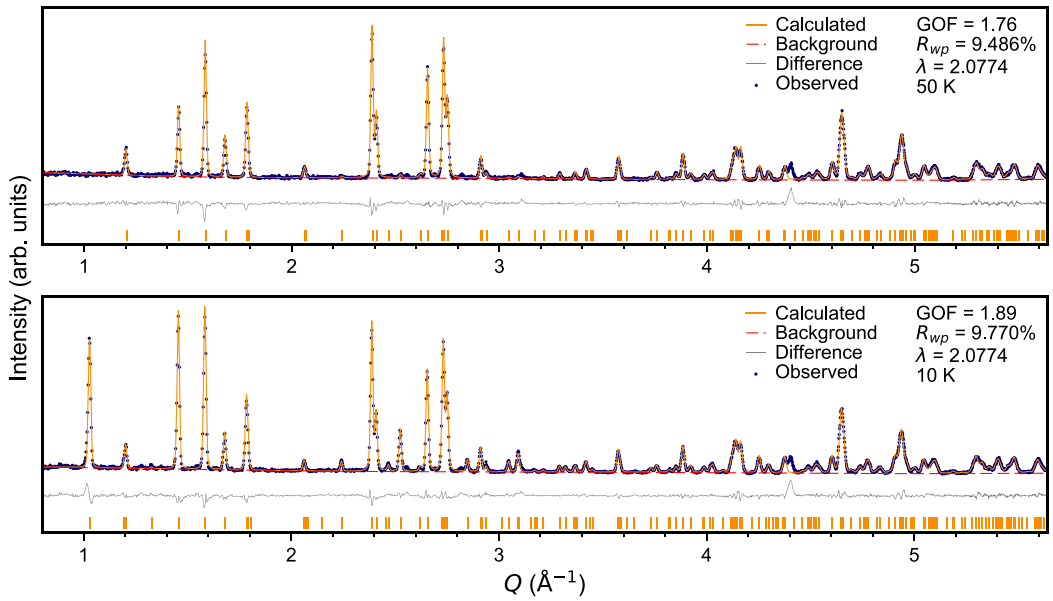

Figure 8. Refinements of the nuclear and magnetic structures with neutron powder diffraction data of $LiMnPO_4$ above and below the ordering temperature.

where β is the critical exponent of the order parameter. We fit our data sets presented in Figure 6 according to the form of the order parameter:

$$I = I_0\left(1 - \frac{T}{T_N}\right)^{2\beta} \tag{3}$$

Note, for $LiCoPO_4$ we excluded the data points at 5 and 10 K from the calculation to better model the function at the transition. Likewise, for $LiMnPO_4$ we excluded the data points at 10, 15, 20, and 50 K. The fitted parameters for $LiCoPO_4$ were T_N = 21.71(7) and β = 0.21(4) and for $LiMnPO_4$ were T_N = 33.7(2) and β = 0.31(3).

For $LiCoPO_4$, T_N = 21.71(7) K is in good agreement with single crystal diffraction experiments on $LiCoPO_4$ performed by Vaknin et al.[28] They measured the (200) and (010) reflections and observed an onset temperature just below 21 K. Our order parameter for $LiCoPO_4$ (β = 0.21(4)) is in agreement with theirs ($\approx$ 0.218) and suggests intermediate behavior between a 2D and 3D Ising system. A more recent single crystal experiment was performed by Fogh et al.[29] They fit the (100) and (301) reflections, and the model gave T_N = 21.55(2) K and β = 0.34(1) under no applied field. This β is closer to what would be expected for a 3D Ising system (β = 0.326).[42] When they applied a 10 T field, β varied only slightly

https://dx.doi.org/10.1021/acs.inorgchem.9b03545
Inorg. Chem. XXXX, XXX, XXX−XXX

(β = 0.30(1)) and the transition temperature decreased to T_N = 17.51(2).

The temperature dependence of the (010) reflection for $LiMnPO_4$ has been measured on a single crystal by Li et al.[43] and Toft-Petersen et al.[40] Our value of T_N = 33.7(2) K is in good agreement with theirs (T_N = 33.9(1) K and 33.40(1) K, respectively). However, our order parameter β = 0.31(3) suggests 3D Ising behavior, whereas their order parameters β = 0.126(17)[43] and β = 0.150(3)[40] suggest 2D Ising behavior. The order parameter for an ideal 2D Ising system is β = 0.125.[42] The error on our calculated value is an order of magnitude greater than theirs due to the number of data points we collected. The differences could arise from either an insufficient number of data points or from differences between single crystal and polycrystalline samples.

Magnetic Structure Analysis. Representational analysis was carried out on the observed reflections in the 10 K neutron powder diffraction patterns to perform a refinement of their observed magnetic structure (see Figures 7 and 8). Indexing was performed in GSAS-II, with predicted magnetic reflections determined using *k*-SUBGROUPSMAG. All reflections were reconciled with a propagation vector k = 0,0,0. We therefore considered models for commensurate order.

In the crystal structure of $LiCoPO_4$ and $LiMnPO_4$, the transition metal cation (M^{2+}) sites are on the 4*c* Wyckoff position. If we model the crystal structure above the transition as a paramagnet, we assign the magnetic space group *Pnma*1′. This group contains every generating element of *Pnma* plus the product of every element and time inversion symmetry 1′. Based upon the gradual onset of ordering below its transition temperature, we assume these materials undergo a continuous Landau-type phase transition. Therefore, the magnetic moments will order according to the symmetry of one maximal subgroup of *Pnma*1′ corresponding to the action of a single order parameter.[44] Given these conditions, we obtain the symmetry mode decomposition for *Pnma*1′ from *k*-SUBGROUPSMAG in the Bilbao Crystallographic Server[45] or from SARA*h* - web representational analysis:[46]

$$\Gamma_{M^{2+}}(4c) = 1\Gamma_1^{+(1)} \oplus 2\Gamma_1^{-(1)} \oplus 2\Gamma_2^{+(1)} \oplus 1\Gamma_2^{-(1)} \oplus 2\Gamma_3^{+(1)} \oplus 1\Gamma_3^{-(1)} \oplus 1\Gamma_4^{+(1)} \oplus 2\Gamma_4^{-(1)} \quad (4)$$

This produces eight one-dimensional irreducible coset representations (IRs). The expression communicates the number of times each IR occurs in the magnetic representation $\Gamma_{M^{2+}}$ (in this case either once or twice). This gives a total of 12 basis vectors (or symmetry modes).

The adopted notation for the representations corresponds to the listings developed by Stokes and Campbell et al. used in *k*-SUBGROUPSMAG.[47] For example, mGM1-(1) corresponds to our notation Γ_1^-. The superscript denotes *gerade* (+) or *ungerade* (−) with respect to spatial inversion. The numeral in parentheses is the order (or dimension) of the representation. Since all the representations are one-dimension in this case, the (1) is omitted from the tables later in the text. See Table S1 for the character table.

The magnetic space groups corresponding to each irreducible representation are listed in Table 3. In GSAS-II, the irreducible representations are computed using *k*-SUBGROUPSMAG during the indexing process,[45] and favorable candidates are saved for later use during refinement. The basis vectors are projected from each IR, indicating along which crystallographic directions the spins are nonzero. In GSAS-II, this is displayed when the user makes a crystallographic phase magnetic and selects one of the candidate magnetic models.

Table 3. Magnetic Symmetry Associated with the Eight Irreducible Representations of the Parent Paramagnetic Space Group *Pnma*1′

IR[a]	MSG[b]	MPG[c]	BVC[d]	MO[e]
Γ_1^+	*Pnma*	*mmm*	A_y	AFM
Γ_2^+	*Pn′m′a*	*m′m′m*	$A_x + F_z$	FM
Γ_3^+	*Pnm′a′*	*mm′m′*	$F_x + A_z$	FM
Γ_4^+	*Pn′ma′*	*m′mm′*	F_y	FM
Γ_1^-	*Pn′m′a′*	*m′m′m′*	$C_x + G_z$	AFM
Γ_2^-	*Pnma′*	*mmm′*	C_y	AFM
Γ_3^-	*Pn′ma*	*m′mm*	G_y	AFM
Γ_4^-	*Pnm′a*	*mm′m*	$G_x + C_z$	AFM

[a]Irreducible representation, superscript + indicates gerade, superscript − indicates ungerade with respect to spatial inversion symmetry. [b]Magnetic space group. [c]Magnetic point group. [d]Basis vector components of the spin modes, which are defined as (F = ↑↑↑↑), (G = ↑↓↑↓), (C = ↑↑↓↓), and (A = ↑↓↓↑) for the four magnetic atoms. The subscripts x, y, and z correspond to the a, b, and c crystallographic directions, respectively. [e]Magnetic order.

In the output of SARA*h*, the basis vectors for each of the spin components are given for each atom on the given Wyckoff position (4*c*). The positions of the four atoms are defined to be 1(x, (1/4), z), 2($-x$ + (1/2), (3/4), z + (1/2)), 3($-x$, (3/4), z + (1/2)), 4(x + (1/2), (1/4), $-z$ + (1/2)) . Using Bertaut's convention, the various configurations are represented by a letter. For instance, if there is a basis vector where the sign for every odd atom is positive and every even atom is negative, it is given the letter (G = ↑↓↑↓) . Additional configurations observed in this space group are (F = ↑↑↑↑), (C = ↑↑↓↓), and (A = ↑↓↓↑). Table 3 lists whether each configuration of spins is ferromagnetic (FM) or antiferromagnetic (AFM). Since the Weiss temperatures determined from the Curie−Weiss analysis were negative—indicating the long-range ordering is antiferromagnetic—we consider fully compensated spin configurations (Table 1).

The observed magnetic reflections also narrow the list of candidate irreducible representations. For $LiMnPO_4$, we observe a strong (010) reflection, but not for $LiCoPO_4$ (Figure 5). Magnetic scattering intensity is only observed when the scattering vector is perpendicular to the magnetic moment. Therefore, the spins for $LiMnPO_4$ are not expected to be aligned along the b axis, suggesting either Γ_1^- or Γ_4^-. For $LiCoPO_4$, the opposite is true and we therefore consider Γ_2^- and Γ_3^-.

The starting structural models for the 10 K refinements were the refined structures from above the transition temperature. The aforementioned models for the magnetic spin modes were tested, and the best fit for $LiMnPO_4$ was obtained with Γ_1^- (Figure 8). Note, while a magnetic moment is allowed by symmetry to be canted in the ac plane according to the spin configuration $C_x + G_z$ (see Table 4), the error in the refined moment along the z axis was higher than the small refined value. Therefore the magnetic component along the z axis was set to zero before completing the refinement, with the observed spin configuration described as C_x. The best model for $LiCoPO_4$ was with Γ_2^- (Figure 8). The refined magnetic parameters are included in Table 5.

https://dx.doi.org/10.1021/acs.inorgchem.9b03545
Inorg. Chem. XXXX, XXX, XXX−XXX

Table 4. Theoretical Magnetic Moment Values for $LiCoPO_4$ and $LiMnPO_4$[48]

	$LiCoPO_4$	$LiMnPO_4$
el. config.[a]	d^7: $t_{2g}^5\ e_g^2$	d^5: $t_{2g}^3\ e_g^2$
	$S = 3/2$	$S = 5/2$
	$L = 3$	$L = 0$
term sym.[b]	^4F	^6S
μ_{L+S} (μ_B)[c]	5.2	5.9
μ_S (μ_B)[d]	3.9	5.9
m (μ_B)[e]	3	5

[a]Electronic configuration. [b]Free ion ground term symbol. [c]$\mu_{L+S} = \sqrt{4S(S+1) + L(L+1)}$. [d]$\mu_S = 2\sqrt{S(S+1)}$. [e]$m = gS$

Table 5. Magnetic Model and Parameters Deduced from Rietveld Refinement of Neutron Powder Diffraction Patterns Taken at 10 K

	$LiCoPO_4$	$LiMnPO_4$
IR	Γ_2^-	Γ_1^-
MSG	$Pnma'$	$Pn'm'a'$
MPG	mmm'	$m'm'm'$
BVCom	C_y	$C_x + G_z$
obsd BVCom[a]	C_y	C_x
all. MMCom[b]	M_y	M_x, M_z
obsd MMCom[c]	M_y	M_x
ref MMCom[d]	3.28(4)	4.28(3)

[a]Observed basis vector components. [b]Allowed magnetic moment components. [c]Observed magnetic moment components. [d]Refined magnetic moment magnitudes.

Using the notation of Gallego et al., the symmetry breaking transition for $LiCoPO_4$ can be expressed as[49]

$$Pnma1' \rightarrow Pnma'(\mathbf{a}, \mathbf{b}, \mathbf{c}; 0, 0, 0) \quad (5)$$

with no transformation of the basis. Likewise, the transition for $LiMnPO_4$ is

$$Pnma1' \rightarrow Pn'm'a'(\mathbf{a}, \mathbf{b}, \mathbf{c}; 0, 0, 0) \quad (6)$$

These results are in agreement with the original magnetic structure determinations by Santoro and Newnham and their colleagues in the 1960s.[24−26]

The refined atomic moment was $gS = 3.28(4)\ \mu_B$ (10 K) per magnetic ion for $LiCoPO_4$. Previous studies on single crystals of $LiCoPO_4$ gave a refined moment of 4.2 μ_B (10 K)[28] and 3.54(5) μ_B (2 K).[29] Santoro and Newnham et al. did not report a refined moment in their work.[25] Based upon high field magnetization studies, the saturated magnetic moment for $LiCoPO_4$ in its fully paramagnetic state has been reported as 3.6 μ_B/ion.[50] Therefore, a magnetic moment as high as 4.2 μ_B is implausible. We note the calculated moment in ref 28 relied heavily upon the (200) and very weak (010) reflection intensities. In the recent 2019 study,[29] the intensities of the 130 commensurate magnetic reflections were normalized to 241 nuclear Bragg reflections, giving the much lower 3.54(5) μ_B. Likewise, our moment 3.28(4) μ_B was computed from normalizing the intensities of 156 commensurate magnetic reflections to 124 nuclear Bragg reflections. Using such a large number of reflections ensures the scale factor used for the refinement is reliable. Therefore, both this work and ref 29 confirm there is partially unquenched orbital angular momentum contributing to the moment, but not as high as the previously reported 4.2 μ_B.[28]

For $LiMnPO_4$, the refined magnetic moment is $gS = 4.28(3)\ \mu_B$ (10 K). This value is much lower than the 5.2 μ_B (6 K) Santoro and Newnham reported.[24,26] Recently, Urusova and colleagues reported neutron powder diffraction data of $LiMnPO_4$ obtained at six temperatures from 2 to 37 K.[37] They also modeled the magnetic structure as antiferromagnetic with the moments aligned along the a axis. They did not include a discussion of representational analysis, nor which type of antiferromagnetic ordering they selected. However, they reported their refined moment as 4.0 μ_B (3.5 K), closer to ours. Our refinement used the intensities from 163 commensurate magnetic reflections and 130 nuclear Bragg reflections for the magnetic structure refinement.

Field-dependent single crystal measurements also observe a moment close to 4 μ_B for $LiMnPO_4$. Toft-Petersen, Vaknin, and their respective colleagues performed a refinement of the single crystal structure at 2 K under an applied field of 4.5 T.[40] In their refinement, they obtained a model with the spin mode $C_z + F_x$, where the antiferromagnetic moment along the c axis is 3.93(3) μ_B, and the field-induced ferromagnetic component along the a axis is 0.37(6) μ_B. This would give a vector sum of about 3.95(9) μ_B (2 K), still much less than Santoro and Newnham's value.

DISCUSSION

Observed Effective and Magnetic Moments. The Curie−Weiss parameters for $LiCoPO_4$ (Table 1) are in good agreement with other literature. The Néel temperature for $LiCoPO_4$ is consistently reported around 22−23 K,[25,28,51−54] which is in good agreement with ours at 22(2) K for the hydrothermal sample and 24(2) K for the solid state sample (Table 1). The effective moment in polycrystalline samples has been reported as low as 4.77 μ_B[53] and as high as 5.7(1) μ_B.[25] Our values lie in between at 5.4(1) μ_B for the hydrothermal sample and 5.1(1) μ_B for the solid state sample. Both are in good agreement with the theoretical model for an effective moment with unquenched orbital angular momentum 5.2 μ_B (Table 4). In all reports, the Curie−Weiss temperature is negative, indicative of antiferromagnetic order.[25,28,51−54] However, measurements with single crystals reveal strong single ion anistropy in the system, which makes more detailed analysis of the exchange in the system unreliable.[28,51,54]

The Curie−Weiss parameters for $LiMnPO_4$ (Table 1) are also in good agreement with other reports.[26,55−58] The transition temperature is reported around 34−35 K, in good agreement with 34(2) K for the hydrothermal sample and 36(2) K for the solid state sample. The effective moment in the literature is reported between 5.82(2) μ_B[56] and 6.1(1) μ_B,[55] close to the theoretical effective moment 5.9 μ_B. Our hydrothermal sample is in good agreement with this at 5.91(2) μ_B, but the value for the solid state sample is low at 5.54(6) μ_B. The sign of θ_{CW} is indicative of antiferromagnetic order.

Field Dependence Observed in the Magnetic Susceptibility. *$LiMnPO_4$.* Our results revealed different synthetic methods varied the features in the $\chi(T)$ curves of $LiMnPO_4$. Notable features included the FC/ZFC bifurcation and apparent shift in the transition temperature for the solid state sample. We therefore discuss our results by comparing both the experimental conditions and synthetic conditions used in other researchers' reports.

Other groups have also observed FC/ZFC bifurcation in their polycrystalline samples around 42−43 K at low fields

https://dx.doi.org/10.1021/acs.inorgchem.9b03545
Inorg. Chem. XXXX, XXX, XXX−XXX

(100 and 200 Oe, respectively).[31,56,59] Arčon et al. used a sol−gel method with high temperature annealing, and Kellerman et al. utilized ceramic sintering. They also observed prominent hysteresis with a coercive field around 1 kOe and 200 Oe, respectively. On the contrary, we observe a very weak signal in the solid state sample (Figure 4) and cannot even assign a coercive field for the hydrothermal sample (Figure S3). Since this hysteresis varies with different samples, this is evidence the signal could be from manganese oxide impurities.

The FC/ZFC bifurcation is likely intrinsic to the $LiMnPO_4$ system, but not around 42 K. Bozorth and Kramer were the first to report a Néel temperature of 42 K for $LiMnPO_4$ in 1959.[60] However, their sample was a mineral and contained about 30% iron substitution on the manganese sites. The transition temperature is coincidentally about 42 K in that composition.[57] Subsequently reported measurements on single crystals and ground single crystals confirm the Néel temperature should be around 34−35 K for $LiMnPO_4$.[26,43,55,58] In addition, neutron diffraction data in this work and elsewhere corroborate ∼34 K is the true zero-field ordering temperature.[40,43]

The most likely impurity in polycrystalline samples is ferrimagnetic Hausmannite (Mn_3O_4), which also has a transition temperature around 42 K.[61] It exhibits a sinusoidal incommensurate structure down to a second transition at 33 K, after which it exhibits commensurate ferrimagnetic ordering down to base temperature.[62−64] The uncompensated magnetic component is the reason for the ferrimagnetic signal in the magnetic susceptibility.[65] Interestingly, that signal is strongly field-dependent, and the second transition at 33 K can only be observed at low applied fields (200 Oe).[65]

Given Arčon and Kellerman used high-temperature sintering in their synthesis, it would be unsurprising for low levels of manganese oxide impurities to be present. Manganese oxides are invariably formed in divalent manganese samples sintered at high temperatures, even prepared under an inert atmosphere.[66] In particular, Hausmannite (Mn_3O_4) exhibits an almost identical bifurcation at 42 K as long as the particle size is large (>15 nm).[67−70] In our own research, we have observed that when care is not taken during synthesis, dark gray impurities are clearly visible on the surface of the light tan sample. Hausmannite is black, supporting this hypothesis. Yet despite our sample containing no physically visible impurity, we still observed the same FC/ZFC bifurcation at 42 K at 1 kOe and below. This suggests even trace impurities can be misleading by obscuring the intrinsic signal from $LiMnPO_4$.

The FC/ZFC bifurcation is also impacted by the strength of the applied field. Kellerman and colleagues performed additional temperature-dependent measurements at several different applied fields up to 5 T. Their results reveal the bifurcation is suppressed above ∼0.8 T. This is consistent with our results, where it is suppressed in the measurements taken at 1 T (10 kOe).

Synthesis conditions also play in the observed bifurcation. For example, Yamada et al. reported bifurcation in their samples sintered below 500 °C, but not at 700 °C.[57] Coincidentally their reported measurements were also performed with a 1 kOe applied field. They attribute this discrepancy to sample quality. However, the high applied field also likely suppressed the bifurcation in their measurements. A better indicator of their sample quality was the cusp of $\chi(T)$, which was close to 35 K.[57] This is in contrast to Kellerman's measurements, in which the Néel temperature remained the same for all applied fields (around 43 K).[31]

In our own solid state measurements, the cusp appears to shift from 42 K at 100 Oe to around 36 K at 10 kOe (Figure 2). The shift closer to the true transition temperature occurs because the antiferromagnetic signal becomes more prominent at higher fields, not because it is actually shifting. Therefore, our and Yamada's samples exhibited a cusp close to 35 K at 1 kOe applied field, while Kellerman's samples with higher levels of impurities remained centered around 42 K.

Our hydrothermal measurements further support this conclusion, since we do not observe a signal around 42 K (Figure 2). The cusp of the susceptibility is centered around 34 K at all fields. Since the hydrothermal samples were synthesized at low temperatures and never annealed, they likely do not contain the same manganese oxide impurities. We also believe the prominent upturn in the susceptibility of the hydrothermal sample below 10 K is due to the paramagnetic signal dominanting over the antiferromagnetic one as the measurement approaches 2 K (Figure S2).

We conclude by emphasizing polycrystalline $LiMnPO_4$ prepared by high temperature sintering or annealing readily produces ferrimagnetic oxide impurities (likely Hausmannite) which can obscure the intrinsic behavior of $LiMnPO_4$. Further studies with single crystals would provide decisive clarity on any proposed weak ferromagnetic ground state proposed by Arčon and others.[56,59]

$LiCoPO_4$. The transition temperature for $LiCoPO_4$ is less contentious. All reports of the magnetic susceptibility assign it between 21 and 23 K.[25,27,28,51−54,71] This is consistent with our measurements, within error (Table 1). However, in hydrothermal $LiCoPO_4$, the cusp of the susceptibility appears to shift about two degrees higher as the applied field is increased.

We are not the first to observe shifts in the observed transition temperature. Kharchencko et al. have observed that the magnitude of the temperature-dependent susceptibility was highly field-dependent in a single crystal of $LiCoPO_4$, having measured under fields as low as 50 Oe and as high as 5 T.[72] They also observed slight hysteresis below the Néel temperature, which they ascribed to a weak ferromagnetic ground state.[27] We did observe a slight bifurcation in FC and ZFC measurements for the hydrothermal sample, but not for the solid state sample.

Our solid state $LiCoPO_4$ exhibited conventional behavior for an antiferromagnet. This is unsurprising as divalent cobalt is less susceptible to oxidation during ceramic synthesis. Indeed, we performed our synthesis under ambient atmosphere.

Like the $LiMnPO_4$ samples, the hydrothermal $LiCoPO_4$ sample exhibited FC/ZFC bifurcation. The behavior observed in the hydrothermal $LiCoPO_4$ is either due to an antiferromagnetic impurity whose transition temperature is around 20 K or is intrinsic to the hydrothermal samples. Intrinsic effects could be due to their particle size effects, which have been observed in Co_3O_4, just as with Mn_3O_4.[73−75] In addition to FC/ZFC bifurcation, the observed transition temperature is impacted by particle morphology and size.

Our hydrothermal synthesis was performed at relatively low temperatures (200 °C) and not annealed. While the finest particles would have been removed during washing and filtration, it is likely they were still finer than the solid state samples. This is supported by XRD data, where the reflections for the hydrothermal samples were slightly broader and less intense than the solid state samples (Figure S1). As with the

https://dx.doi.org/10.1021/acs.inorgchem.9b03545
Inorg. Chem. XXXX, XXX, XXX−XXX

$LiMnPO_4$ samples, this anomalous behavior was suppressed at higher fields.

Comparison of Magnetic Structures. We present the refined structural models from neutron powder diffraction data in Figure 9. The visualizations were created using the modeling software *VESTA 3*.[18]

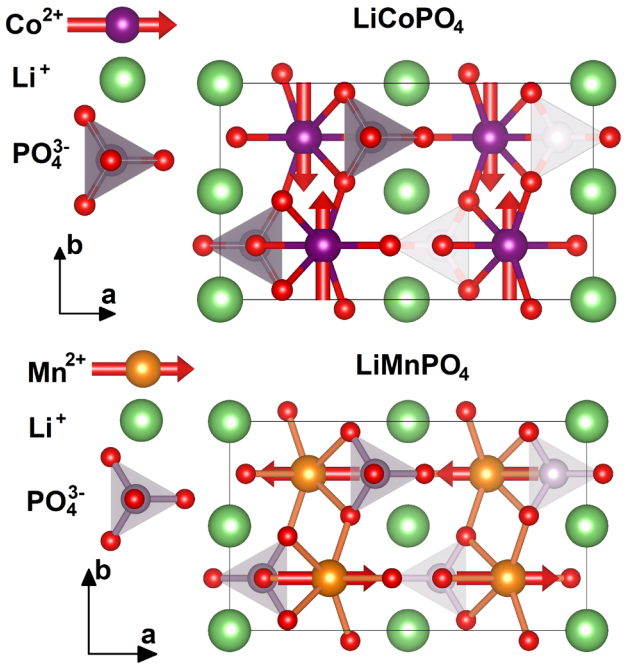

Figure 9. Magnetic structure model of $LiCoPO_4$ and $LiMnPO_4$ able to be resolved from powder neutron powder diffraction.

For $LiMnPO_4$, the refined magnetic structure is in good agreement with all previously reported works.[24,26,37,40] However, the refined magnetic moment of 4.28(3) μ_B is much lower than the 5.2 μ_B in Newnham and Santoro's first report. As discussed previously, the effective moment determined from magnetic susceptibility agreed well with expected values. This suggests that the cause for the moment reduction does not impact the ion's response to an applied field. Rather, the neutron diffraction experiment is unable to model the full spontaneous magnetization of the lattice under zero applied field.

One explanation for the low refined moment is covalency between the Mn^{2+} ion with the surrounding O^{2-} ligands. The effective moment determined from Curie–Weiss analysis is nearly 5.9 μ_B, which is characteristic of high-spin d^5 centers. Since all of the orbitals for Mn^{2+} are only half filled, they are all available for bonding with the surrounding ligands. As a result, the covalency reduces the total moment size by nearly 16%. The covalency also alters the localized spin density at the Mn site and therefore its magnetic form factor. We note the Néel temperature is higher for the manganese analog than the cobalt or nickel analogs. The higher temperature is a manifestation of the increased exchange interactions between the magnetic ions, which is strengthened in the $LiMnPO_4$ by the bond covalency.

The magnetic moment for $LiCoPO_4$ refined to 3.28(4) μ_B. This is higher than the expected 3 μ_B due to some degree of unquenched orbital angular momentum. This observation is consistent with the measurements of the effective moment.

Recall, for $LiCoPO_4$ we did not observe any intensity for the (010) reflection, and this was decisive in our assignment of the Γ_2^- representation, corresponding to *Pnma′* (*mmm′*). However, Vaknin et al. did observe a weak (010) reflection in their measurement on a single crystal.[28] Based upon this, they concluded there was a small rotational component off the *b* axis by 4.6°. They suggested the lower-symmetry magnetic point group would need to exhibit the same magneto-electric tensor components as the previously determined *mmm′* (from *Pnma′*), and possibly additional components. They also cited Kharchenko and colleague's work, observing a weak ferromagnetic component in magnetic susceptibility measurements on a single crystal, suggesting either the point group 2′ or *m′*.[27] Based upon this, Vaknin et al. concluded the off-axis rotation leads to the point group $2'_x/m_y$, and the weak ferromagnetic component further reduces the symmetry to $2'_x$. Second-harmonic generation spectroscopy measurements by Fiebig et al. further supported the conclusion that the lower point group is $2'_x$.[19,21]

More recently Fogh, Vaknin, Toft-Petersen, and their colleagues performed meticulous neutron diffraction experiments on their own single crystal and were unable to observe the (010) reflection.[29] They did observe a weak reflection at (100) suggesting an additional A_z component with a canting angle of 7(1)°. The rotation leads to the point group $2_z/m'_z$, and the weak ferromagnetic moment reduces the symmetry to m'_z. This alternate explanation is consistent with both Vaknin et al.'s and Kharchencko et al.'s earlier results,[27,28] but not the second harmonic generation results by Fiebig and colleagues.[19,21]

We observed neither the (010) nor (100) reflection in this study on $LiCoPO_4$ since this experiment was with a powder sample. Indeed, Fogh and colleagues explained they were unable to observe any evidence of magnetic structure beyond that of *mmm′* in the preliminary measurements on their crystal. They were only able to observe the weak reflections from the canted structure on an instrument with a lower background.[29] We therefore only offer confirmation that the ordering is primarily described by C_y (*Pnma′*, *mmm′*).

CONCLUSIONS

We synthesized $LiCoPO_4$ and $LiMnPO_4$ by hydrothermal and ceramic methods. The magnetic susceptibility differs for each composition and in samples prepared by different methods. In particular, we observe evidence of Hausmannite (Mn_3O_4) in the $LiMnPO_4$ sample synthesized by high temperature ceramic sintering. In addition, there is noticeable bifurcation between the FC and ZFC curves in the solid state $LiMnPO_4$ sample and the hydrothermally prepared samples. The bifurcation could also be the result of an unidentified impurity, or it could be due to particle size effects. Regardless, at high applied fields these features are suppressed, resulting in reasonable Curie–Weiss parameters in good agreement with the literature. This demonstrates that the observed behavior is strongly field-dependent at low fields (below 10 kOe).

We also performed neutron powder diffraction measurements on the samples prepared via solid state methods. The fitted order parameter for the observed magnetic reflections for $LiMnPO_4$ is characteristic of a 3D Ising system; our fitted order parameter for $LiCoPO_4$ suggests intermediate behavior between a 2D and 3D Ising model. Since the data were on a polycrystalline sample, we are unable to observe low-intensity reflections that could indicate slight canting or spin rotation.

https://dx.doi.org/10.1021/acs.inorgchem.9b03545
Inorg. Chem. XXXX, XXX, XXX–XXX

The magnetic structure models are only able to confirm the primarily *C*-type antiferromagnetic order along the *y* axis for $LiCoPO_4$ and along the *x* axis for $LiMnPO_4$. Neither spin canting nor rotation are observed. Although there is considerable disagreement in past literature on the moment size for both compounds, our analysis is consistent with a moment size of 3.28(4) μ_B for Co^{2+}, indicative of orbital contribution to its total moment, and 4.28(3) μ_B for Mn^{2+}, which we attribute to the high degree of covalency in the Mn−O bond.

■ ASSOCIATED CONTENT

Supporting Information

The Supporting Information is available free of charge at https://pubs.acs.org/doi/10.1021/acs.inorgchem.9b03545.

Character table for *Pnma*1′, refined structural parameters and bond angles/lengths for $LiCoPO_4$ and $LiMnPO_4$ NPD data, preliminary refinements for $LiCoPO_4$ and $LiMnPO_4$ XRD data, and additional plots of hydrothermal $LiMnPO_4$, solid state $LiCoPO_4$, and solid state $LiMnPO_4$ susceptibility data (PDF)

Supporting Information TEX files (ZIP)

■ AUTHOR INFORMATION

Corresponding Author

Efrain E. Rodriguez − *Department of Chemistry and Biochemistry, University of Maryland, College Park, Maryland 20742, United States;* orcid.org/0000-0001-6044-1543; Email: efrain@umd.edu

Author

Stephanie Gnewuch − *Department of Chemistry and Biochemistry, University of Maryland, College Park, Maryland 20742, United States;* orcid.org/0000-0002-2050-7189

Complete contact information is available at: https://pubs.acs.org/10.1021/acs.inorgchem.9b03545

Notes

The authors declare no competing financial interest.

■ ACKNOWLEDGMENTS

Funding for this project is supported by the U.S. Department of Energy, Office of Science, Office of Basic Energy Sciences under Award Number DE-SC0016434. We acknowledge support of the National Institute of Standards and Technology, U.S. Department of Commerce, in providing the neutron research facilities used in this work. In particular, we thank Craig Brown for beamline support. We also acknowledge support from the Center for Nanophysics and Advanced Materials.

■ REFERENCES

(1) Mauger, A.; Julien, C. M. Olivine positive electrodes for Li-ion batteries: Status and perspectives. *Batteries* **2018**, *4*, 39.

(2) Goodenough, J. B. Evolution of strategies for modern rechargeable batteries. *Acc. Chem. Res.* **2013**, *46*, 1053−1061.

(3) Zhang, M.; Garcia-Araez, N.; Hector, A. L. Understanding and development of olivine $LiCoPO_4$ cathode materials for lithium-ion batteries. *J. Mater. Chem. A* **2018**, *6*, 14483−14517.

(4) Melot, B. C.; Tarascon, J. M. Design and preparation of materials for advanced electrochemical storage. *Acc. Chem. Res.* **2013**, *46*, 1226−1238.

(5) Wang, J.; Sun, X. Olivine $LiFePO_4$: The remaining challenges for future energy storage. *Energy Environ. Sci.* **2015**, *8*, 1110−1138.

(6) Aravindan, V.; Gnanaraj, J.; Lee, Y. S.; Madhavi, S. $LiMnPO_4$ - A next generation cathode material for lithium-ion batteries. *J. Mater. Chem. A* **2013**, *1*, 3518−3539.

(7) Padhi, A. K.; Nanjundaswamy, K. S.; Goodenough, J. B. Phospho-olivines as Positive-Electrode Materials for Rechargeable Lithium Batteries. *J. Electrochem. Soc.* **1997**, *144*, 1188−1194.

(8) Ederer, C.; Spaldin, N. A. Towards a microscopic theory of toroidal moments in bulk periodic crystals. *Phys. Rev. B: Condens. Matter Mater. Phys.* **2007**, *76*, 214404.

(9) Spaldin, N. A.; Fiebig, M.; Mostovoy, M. The toroidal moment in condensed-matter physics and its relation to the magnetoelectric effect. *J. Phys.: Condens. Matter* **2008**, *20*, 434203.

(10) Scaramucci, A.; Bousquet, E.; Fechner, M.; Mostovoy, M.; Spaldin, N. A. Linear magnetoelectric effect by orbital magnetism. *Phys. Rev. Lett.* **2012**, *109*, 1−5.

(11) Spaldin, N. A.; Fechner, M.; Bousquet, E.; Balatsky, A.; Nordström, L. Monopole-based formalism for the diagonal magnetoelectric response. *Phys. Rev. B: Condens. Matter Mater. Phys.* **2013**, *88*, 094429.

(12) Bertaut, E.; Mercier, M. Magnetoelectricity in Theory and Experiment. *Mater. Res. Bull.* **1971**, *6*, 907−922.

(13) Mercier, M. Une propriété nouvelle des matériaux magnétiques: l'effet magnétoélectrique. *Revue générale de l'électricité* **1971**, *80*, 143−152.

(14) Wells, A. F. *Structural Inorganic Chemistry*, 5th ed.; Oxford University Press: New York, 1984; Chapter Complex Oxides, pp 575−625.

(15) Greenwood, N.; Earnshaw, A. *Chemistry of the Elements*, 1st ed.; Pergamon Press: New York, 1984; Chapter Silicon, pp 379−426.

(16) Liu, C.; Neale, Z. G.; Cao, G. Understanding electrochemical potentials of cathode materials in rechargeable batteries. *Mater. Today* **2016**, *19*, 109−123.

(17) Dai, D.; Whangbo, M.; Koo, H.-J.; Rocquefelte, X.; Jobic, S.; Villesuzanne, A. Analysis of the Spin Exchange Interactions and the Ordered Magnetic Structures of Lithium Transition Metal Phosphates $LiMPO_4$ (*M* = Mn, Fe, Co, Ni) with the Olivine Structure. *Inorg. Chem.* **2005**, *44*, 2407−2413.

(18) Momma, K.; Izumi, F. VESTA 3 for three-dimensional visualization of crystal, volumetric and morphology data. *J. Appl. Crystallogr.* **2011**, *44*, 1272−1276.

(19) Van Aken, B. B.; Rivera, J.-P.; Schmid, H.; Fiebig, M. Observation of ferrotoroidic domains. *Nature* **2007**, *449*, 702−705.

(20) Van Aken, B. B.; Rivera, J. P.; Schmid, H.; Fiebig, M. Anisotropy of antiferromagnetic 180° domains in $LiCoPO_4$ and $LiNiPO_4$. *Phys. Rev. Lett.* **2008**, *101*, 157202.

(21) Zimmermann, A. S.; Meier, D.; Fiebig, M. Ferroic nature of magnetic toroidal order. *Nat. Commun.* **2014**, *5*, 4796.

(22) Birol, T.; Benedek, N. A.; Das, H.; Wysocki, A. L.; Mulder, A. T.; Abbett, B. M.; Smith, E. H.; Ghosh, S.; Fennie, C. J. The magnetoelectric effect in transition metal oxides: Insights and the rational design of new materials from first principles. *Curr. Opin. Solid State Mater. Sci.* **2012**, *16*, 227−242.

(23) Belashchenko, K. D.; Tchernyshyov, O.; Kovalev, A. A.; Tretiakov, O. A. Magnetoelectric domain wall dynamics and its implications for magnetoelectric memory. *Appl. Phys. Lett.* **2016**, *108*, 132403.

(24) Newnham, R. E.; Santoro, R. P.; Redman, M. Neutron-diffraction study of $LiMnPO_4$. *J. Phys. Chem. Solids* **1965**, *26*, 445−447.

(25) Santoro, R. P.; Segal, D. J.; Newnham, R. E. Magnetic properties of $LiCoPO_4$ and $LiNiPO_4$. *J. Phys. Chem. Solids* **1966**, *27*, 1192−1193.

(26) Santoro, R. P.; Newnham, R. E. Antiferromagnetism in $LiFePO_4$. *Acta Crystallogr.* **1967**, *22*, 344−347.

(27) Kharchenko, N. F.; Kharchenko, Y. N.; Szymczak, R.; Baran, M.; Schmid, H. Weak ferromagnetism in the antiferromagnetic

https://dx.doi.org/10.1021/acs.inorgchem.9b03545
Inorg. Chem. XXXX, XXX, XXX−XXX

magnetoelectric crystal $LiCoPO_4$. *Low Temp. Phys.* **2001**, *27*, 895−898.
(28) Vaknin, D.; Zarestky, J. L.; Miller, L. L.; Rivera, J.-P.; Schmid, H. Weakly coupled antiferromagnetic planes in single-crystal $LiCoPO_4$. *Phys. Rev. B: Condens. Matter Mater. Phys.* **2002**, *65*, 224414.
(29) Fogh, E.; Zaharko, O.; Schefer, J.; Niedermayer, C.; Holm-Dahlin, S.; Sørensen, M. K.; Kristensen, A. B.; Andersen, N. H.; Vaknin, D.; Christensen, N. B.; Toft-Petersen, R. Dzyaloshinskii-Moriya interaction and the magnetic ground state in magnetoelectric $LiCoPO_4$. *Phys. Rev. B: Condens. Matter Mater. Phys.* **2019**, *99*, 104421.
(30) Baker, P. J.; Franke, I.; Pratt, F. L.; Lancaster, T.; Prabhakaran, D.; Hayes, W.; Blundell, S. J. Probing magnetic order in LiMPO4 (*M* = Ni, Co, Fe) and lithium diffusion in Li_xFePO_4. *Phys. Rev. B: Condens. Matter Mater. Phys.* **2011**, *84*, 174403.
(31) Kellerman, D. G.; Chukalkin, Y. G.; Medvedeva, N. I.; Gorshkov, V. S.; Semenova, A. S. Effect of vanadium doping on the magnetic properties of $LiMnPO_4$. *Phys. Status Solidi B* **2016**, *253*, 965−975.
(32) Lu, Z.; Chen, H.; Robert, R.; Zhu, B. Y.; Deng, J.; Wu, L.; Chung, C. Y.; Grey, C. P. Citric acid- and ammonium-mediated morphological transformations of olivine $LiFePO_4$ particles. *Chem. Mater.* **2011**, *23*, 2848−2859.
(33) Manzi, J.; Curcio, M.; Brutti, S. Structural and Morphological Tuning of $LiCoPO_4$ Materials Synthesized by Solvo-Thermal Methods for Li-Cell Applications. *Nanomaterials* **2015**, *5*, 2212−2230.
(34) Brutti, S.; Manzi, J.; De Bonis, A.; Di Lecce, D.; Vitucci, F.; Paolone, A.; Trequattrini, F.; Panero, S. Controlled synthesis of $LiCoPO_4$ by a solvo-thermal method at 220°C. *Mater. Lett.* **2015**, *145*, 324−327.
(35) Cheary, R. W.; Coelho, A. Fundamental parameters approach to x-ray line-profile fitting. *J. Appl. Crystallogr.* **1992**, *25*, 109−121.
(36) Kubel, F. Crystal structure of lithium cobalt double orthophosphate, $LiCoPO_4$. *Z. Kristallogr. - Cryst. Mater.* **1994**, *209*, 755.
(37) Urusova, N. V.; Semkin, M. A.; Lee, S.; Barykina, Y. A.; Kellerman, D. G.; Teplykh, A. E.; Pirogov, A. N.; Volegov, A. S.; Skryabin, Y. N. Magnetic ordering and crystal structure of $LiMPO_4$ compounds with *M* = (Mn, Fe, Ni/Mn, and Ni/Co). *Ferroelectrics* **2017**, *509*, 74−79.
(38) Toby, B. H.; Von Dreele, R. B. GSAS-II: The genesis of a modern open-source all purpose crystallography software package. *J. Appl. Crystallogr.* **2013**, *46*, 544−549.
(39) Vaknin, D.; Zarestky, J. L.; Ostenson, J. E.; Chakoumakos, B. C.; Goñi, A.; Pagliuso, P. J.; Rojo, T.; Barberis, G. E. Weakly (x = 0) and randomly (x = 0.033) coupled Ising antiferromagnetic planes in $(Li_{1-3x}Fe_x)NiPO_4$ compounds. *Phys. Rev. B: Condens. Matter Mater. Phys.* **1999**, *60*, 1100.
(40) Toft-Petersen, R.; Andersen, N. H.; Li, H.; Li, J.; Tian, W.; Bud'ko, S. L.; Jensen, T. B. S.; Niedermayer, C.; Laver, M.; Zaharko, O.; Lynn, J. W.; Vaknin, D. Magnetic phase diagram of magnetoelectric $LiMnPO_4$. *Phys. Rev. B: Condens. Matter Mater. Phys.* **2012**, *85*, 224415.
(41) Li, J.; Garlea, V. O.; Zarestky, J. L.; Vaknin, D. Spin-waves in antiferromagnetic single-crystal $LiFePO_4$. *Phys. Rev. B: Condens. Matter Mater. Phys.* **2006**, *73*, 024410.
(42) Blundell, S. *Magnetism in Condensed Matter*; Oxford University Press, 2011; Chapter Order and Broken Symmetry, pp 111−139.
(43) Li, J.; Tian, W.; Chen, Y.; Zarestky, J. L.; Lynn, J. W.; Vaknin, D. Antiferromagnetism in the magnetoelectric effect single crystal $LiMnPO_4$. *Phys. Rev. B: Condens. Matter Mater. Phys.* **2009**, *79*, 144410.
(44) Ascher, E. Permutation representations, epikernels and phase transitions. *J. Phys. C: Solid State Phys.* **1977**, *10*, 1365−1377.
(45) Perez-Mato, J.; Gallego, S.; Tasci, E.; Elcoro, L.; de la Flor, G.; Aroyo, M. Symmetry-Based Computational Tools for Magnetic Crystallography. *Annu. Rev. Mater. Res.* **2015**, *45*, 217−248.
(46) Wills, A. S. A new protocol for the determination of magnetic structures using simulated annealing and representational analysis (SARA*h*. *Phys. B* **2000**, *276−278*, 680−681.
(47) Stokes, H. T.; Campbell, B. J.; Cordes, R. Tabulation of irreducible representations of the crystallographic space groups and their superspace extensions. *Acta Crystallogr., Sect. A: Found. Crystallogr.* **2013**, *69*, 388−395.
(48) Carlin, R. L. *Magnetochemistry*; Springer-Verlag: New York, 1986; Chapter Paramagnetism and Crystalline Fields: The Iron Series Ions, pp 52−69.
(49) Gallego, S. V.; Perez-Mato, J. M.; Elcoro, L.; Tasci, E. S.; Hanson, R. M.; Momma, K.; Aroyo, M. I.; Madariaga, G. MAGNDATA: Towards a database of magnetic structures. I. the commensurate case. *J. Appl. Crystallogr.* **2016**, *49*, 1750−1776.
(50) Kharchenko, N. F.; Khrustalev, V. M.; Savitskiĭ, V. Magnetic field induced spin reorientation in the strongly anisotropic antiferromagnetic crystal $LiCoPO_4$. *Low Temp. Phys.* **2010**, *36*, 558−564.
(51) Creer, J. G.; Troup, G. J. The Magnetic Susceptibility of $LiFePO_4$ and $LiCoPO_4$. *Phys. Lett. A* **1970**, *32A*, 439−440.
(52) Goñi, A.; Lezama, L.; Barberis, G. E.; Pizarro, J. L.; Arriortua, M. I.; Rojo, T. Magnetic properties of the $LiMPO_4$, (*M* = Co, Ni) compounds. *J. Magn. Magn. Mater.* **1996**, *164*, 251−255.
(53) Singh, V.; Gershinsky, Y.; Kosa, M.; Dixit, M.; Zitoun, D.; Major, D. T. Magnetism in olivine-type $LiCo_{1-x}Fe_xPO_4$ cathode materials: bridging theory and experiment. *Phys. Chem. Chem. Phys.* **2015**, *17*, 31202−31215.
(54) Fogh, E.; Toft-Petersen, R.; Ressouche, E.; Niedermayer, C.; Holm, S. L.; Bartkowiak, M.; Prokhnenko, O.; Sloth, S.; Isaksen, F. W.; Vaknin, D.; Christensen, N. B. Magnetic order, hysteresis, and phase coexistence in magnetoelectric $LiCoPO_4$. *Phys. Rev. B: Condens. Matter Mater. Phys.* **2017**, *96*, 104420.
(55) Mercier, M.; Bertaut, E.; Quezel, G.; Bauer, P. Interpretation de l'effet magnetoelectrique dans $LiMnPO_4$. *Solid State Commun.* **1969**, *7*, 149−154.
(56) Arčon, D.; Zorko, A.; Dominko, R.; Jagličič, Z. A comparative study of magnetic properties of $LiFePO_4$ and $LiMnPO_4$. *J. Phys.: Condens. Matter* **2004**, *16*, 5531−5548.
(57) Yamada, A.; Takei, Y.; Koizumi, H.; Sonoyama, N.; Kanno, R.; Itoh, K.; Yonemura, M.; Kamiyama, T. Electrochemical, Magnetic, and Structural Investigation of the $Li_x(Mn_yFe_{1-y})PO_4$ Olivine Phases. *Chem. Mater.* **2006**, *18*, 804−813.
(58) Wizent, N.; Behr, G.; Lipps, F.; Hellmann, I.; Klingeler, R.; Kataev, V.; Löser, W.; Sato, N.; Büchner, B. Single-crystal growth of $LiMnPO_4$ by the floating-zone method. *J. Cryst. Growth* **2009**, *311*, 1273−1277.
(59) Arčon, D.; Zorko, A.; Cevc, P.; Dominko, R.; Bele, M.; Jamnik, J.; Jagličić, Z.; Golosovsky, I. Weak ferromagnetism of $LiMnPO_4$. *J. Phys. Chem. Solids* **2004**, *65*, 1773−1777.
(60) Bozorth, R.; Kramer, V. Some ferrimagnetic and antiferromagnetic materials at low temperatures. *J. Phys. Radium* **1959**, *20*, 393−401.
(61) Dwight, K.; Menyuk, N. Magnetic Properties of Mn_3O_4 and the Canted Spin Problem. *Phys. Rev.* **1960**, *119*, 1470.
(62) Boucher, B.; Buhl, R.; Perrin, M. Proprietes et structure magnetique de Mn_3O_4. *J. Phys. Chem. Solids* **1971**, *32*, 2429−2437.
(63) Jensen, G. B.; Nielsen, O. V. The magnetic structure of Mn_3O_4 Hausmannite between 4.7K and the Néel point, 41K. *J. Phys. C: Solid State Phys.* **1974**, *7*, 409−424.
(64) Chardon, B.; Vigneron, F. Mn_3O_4 Commensurate and Incommensurate Magnetic Structures. *J. Magn. Magn. Mater.* **1986**, *58*, 128−134.
(65) Srinivasan, G.; Seehra, M. S. Magnetic properties of Mn_3O_4 and a solution of the canted-spin problem. *Phys. Rev. B: Condens. Matter Mater. Phys.* **1983**, *28*, 1−7.
(66) Thota, S.; Prasad, B.; Kumar, J. Formation and magnetic behaviour of manganese oxide nanoparticles. *Mater. Sci. Eng., B* **2010**, *167*, 153−160.

https://dx.doi.org/10.1021/acs.inorgchem.9b03545
Inorg. Chem. XXXX, XXX, XXX−XXX

(67) Narayani, L.; Jagadeesha Angadi, V.; Sukhdev, A.; Challa, M.; Matteppanavar, S.; Deepthi, P. R.; Mohan Kumar, P.; Pasha, M. Mechanism of high temperature induced phase transformation and magnetic properties of Mn_3O_4 crystallites. *J. Magn. Magn. Mater.* **2019**, *476*, 268−273.
(68) Gopalakrishnan, I. K.; Bagkar, N.; Ganguly, R.; Kulshreshtha, S. K. Synthesis of superparamagnetic Mn_3O_4 nanocrystallites by ultrasonic irradiation. *J. Cryst. Growth* **2005**, *280*, 436−441.
(69) Seo, W. S.; Jo, H. H.; Lee, K.; Kim, B.; Oh, S. J.; Park, J. T. Size-dependent magnetic properties of colloidal Mn_3O_4 and MnO nanoparticles. *Angew. Chem., Int. Ed.* **2004**, *43*, 1115−1117.
(70) Chen, B.; Rao, G.; Wang, S.; Lan, Y.; Pan, L.; Zhang, X. Facile synthesis and characterization of Mn_3O_4 nanoparticles by auto-combustion method. *Mater. Lett.* **2015**, *154*, 160−162.
(71) Fogh, E. Magnetic and magnetoelectric properties of lithium orthophosphates. Ph.D. thesis, Technical University of Denmark, 2018.
(72) Kharchenko, N. F.; Desnenko, V. A.; Kharchenko, Y. N.; Szymczak, R.; Baran, M. Nonmonotonic temperature dependence of the spontaneous magnetization of the antiferromagnetic crystal $LiCoPO_4$. *Low Temp. Phys.* **2002**, *28*, 646−652.
(73) Hill, A. H.; Harrison, A.; Ritter, C.; Yue, W.; Zhou, W. Neutron powder diffraction and magnetic studies of mesoporous Co_3O_4. *J. Magn. Magn. Mater.* **2011**, *323*, 226−231.
(74) Dutta, P.; Seehra, M. S.; Thota, S.; Kumar, J. A comparative study of the magnetic properties of bulk and nanocrystalline Co_3O_4. *J. Phys.: Condens. Matter* **2008**, *20*, 015218.
(75) Sahoo, P.; Djieutedjeu, H.; Poudeu, P. F. Co_3O_4 nanostructures: The effect of synthesis conditions on particles size, magnetism and transport properties. *J. Mater. Chem. A* **2013**, *1*, 15022.

https://dx.doi.org/10.1021/acs.inorgchem.9b03545
Inorg. Chem. XXXX, XXX, XXX−XXX